



MATERIALS SCIENCE

Continuous production of ultratough semiconducting polymer fibers with high electronic performance

Zhi Zhang¹, Peiyun Li¹, Miao Xiong¹, Liang Zhang², Jupeng Chen¹, Xun Lei¹, Xiran Pan¹, Xiu Wang¹, Xin-Yu Deng¹, Weiyu Shen³, Zi Mei¹, Kai-Kai Liu¹, Guangchao Liu¹, Zhen Huang¹, Shixian Lv¹, Yuanlong Shao^{1,2}, Ting Lei^{1*}

Conjugated polymers have demonstrated promising optoelectronic properties, but their brittleness and poor mechanical characteristics have hindered their fabrication into durable fibers and textiles. Here, we report a universal approach to continuously producing highly strong, ultratough conjugated polymer fibers using a flow-enhanced crystallization (FLEX) method. These fibers exhibit one order of magnitude higher tensile strength (>200 megapascals) and toughness (>80 megajoules per cubic meter) than traditional semiconducting polymer fibers and films, outperforming many synthetic fibers, ready for scalable production. These fibers also exhibit unique strain-enhanced electronic properties and exceptional performance when used as stretchable conductors, thermoelectrics, transistors, and sensors. This work not only highlights the influence of fluid mechanical effects on the crystallization and mechanical properties of conjugated polymers but also opens up exciting possibilities for integrating these functional fibers into wearable electronics.

INTRODUCTION

Fibers can be processed into one-dimensional (1D) yarns, 2D fabrics, and 3D spacer fabrics via textile technology, suitable for seamlessly integrated into everyday wearables. Synthetic fibers, such as polyamide or nylon that contain highly crystalline polymer chains and abundant hydrogen bonds, are commonly used, as they offer desirable mechanical properties (strength > 100 MPa) (fig. S1A) (1, 2). Fiber materials have undergone a revolution in recent decades, resulting in the emergence of fiber electronics (3, 4). These electronics offer promising advantages, such as flexibility, wearability, knittability, and implantability (4–6). On the basis of these fibers, functional textiles with hierarchical structures can be designed with multiple functions and high mechanical stretchability.

For electronic fibers, both mechanical properties and electronic performances are crucial. Conventional inorganic electronic fibers based on silicon (Si) (7) and zinc oxide (ZnO) (8) are rigid and brittle, making them unsuitable for continuous production and textile integration. Moreover, their Young's modulus (>100 GPa) are much higher than that of human tissues (0.1 to 100 MPa) (9), making them not suitable for implantable devices. Hydrogel fibers, on the other hand, have good biocompatibility, low Young's modulus, and remarkable elongation. Unfortunately, their weak interchain interactions and high water content limit their mechanical properties (tensile strength of <1 MPa and toughness of <10 MJ m⁻³) (10–12) and make them vulnerable to damage from body motion or tissue movement (fig. S1, A and B). Furthermore, most hydrogels are only ionically conductive and not suitable for constructing high-performance semiconducting devices (13, 14). Recently, a functional soft fiber named PANSion was reported (15). However, its strength (6 MPa) and conductivity (1.82 S m⁻¹) were far from the demands (fig. S1 and

Discussion). Therefore, achieving both high mechanical properties and excellent device performance simultaneously remains a challenge for electronic fibers.

Conjugated polymers (CPs) have received increasing attention due to their high mechanical flexibility, readily structural tunability, and good solution processability, making them suitable for flexible and stretchable electronics, including organic photovoltaics (16), organic field-effect transistors (17), organic thermoelectrics (OTEs) (18), and organic electrochemical transistors (OECTs) (19). To date, only a few conducting polymers, e.g., poly(3,4-ethylenedioxythiophene):polystyrene sulfonate (PEDOT:PSS) (20) and polyaniline (21), can be wet spun into strong fibers (tensile strength of ~100 MPa and stretchability of <30%) by increasing their solution concentrations (> 40 mg ml⁻¹) (fig. S1A). Because of their lack of side chains, these polymers can closely pack and form strong interactions at high concentrations, making them suitable for producing robust fibers. In contrast, semiconducting polymers invariably possess lengthy side chains to enhance solubility and a large number of conformational disorders, making them difficult to process into strong and tough films or fibers. Despite numerous attempts to improve the mechanical properties of semiconducting polymers through molecular design and process engineering (22, 23), their films or fibers still exhibit inadequate mechanical strength, with a tensile strength of only a few tens of megapascals. As a result, they are prone to breaking during continuous production, textile manufacturing, and everyday use. For example, a polymer DPP-C5 with a nonconjugated backbone is used for melt-processing (24), but the resulting fibers only exhibit a moderate tensile strength (15 MPa) and toughness (10 MJ m⁻³). These properties still lag far behind synthetic fibers. Moreover, introducing the nonconjugated backbone interrupts efficient charge transport, resulting in poor electronic performance in the fibers. Therefore, it remains an urgent need and a great challenge to continuously fabricate semiconducting polymers into strong and tough fibers while keeping their electronic performance uncompromised.

Here, we report a general method, namely, flow-enhanced crystallization (FLEX), for the continuous production of semiconducting polymer fibers with exceptional strength, toughness, and

¹Key Laboratory of Polymer Chemistry and Physics of Ministry of Education, School of Materials Science and Engineering, Peking University, Beijing 100871, China.

²College of Energy Soochow Institute for Energy and Materials Innovations (SIEMIS), Jiangsu Provincial Key Laboratory for Advanced Carbon Materials and Wearable Energy Technologies, Soochow University, Suzhou 215006, China. ³College of Engineering, Peking University, Beijing 100871, China.

*Corresponding author. Email: tinglei@pku.edu.cn

stretchability, ideal for high-performance fiber electronics (Fig. 1). Unlike the traditional wet-spinning approach that requires highly concentrated polymer solution to meet the good spinnability, we oppositely lower the polymers' solution concentration to provide adequate space for polymer disaggregation under strong extensional and shear flows, change the fast bidirectional antisolvent

flow to slow unidirectional flow, and use slow post-stretching to further enhance polymer chain alignment and crystallinity (Fig. 1, D and E). This led to the emergence of new crystalline diffraction peaks that have not been observed in thin films. The resulting fibers displayed remarkable mechanical properties that have not been realized in CPs. Furthermore, these fibers exhibited strain-enhanced electronic performance

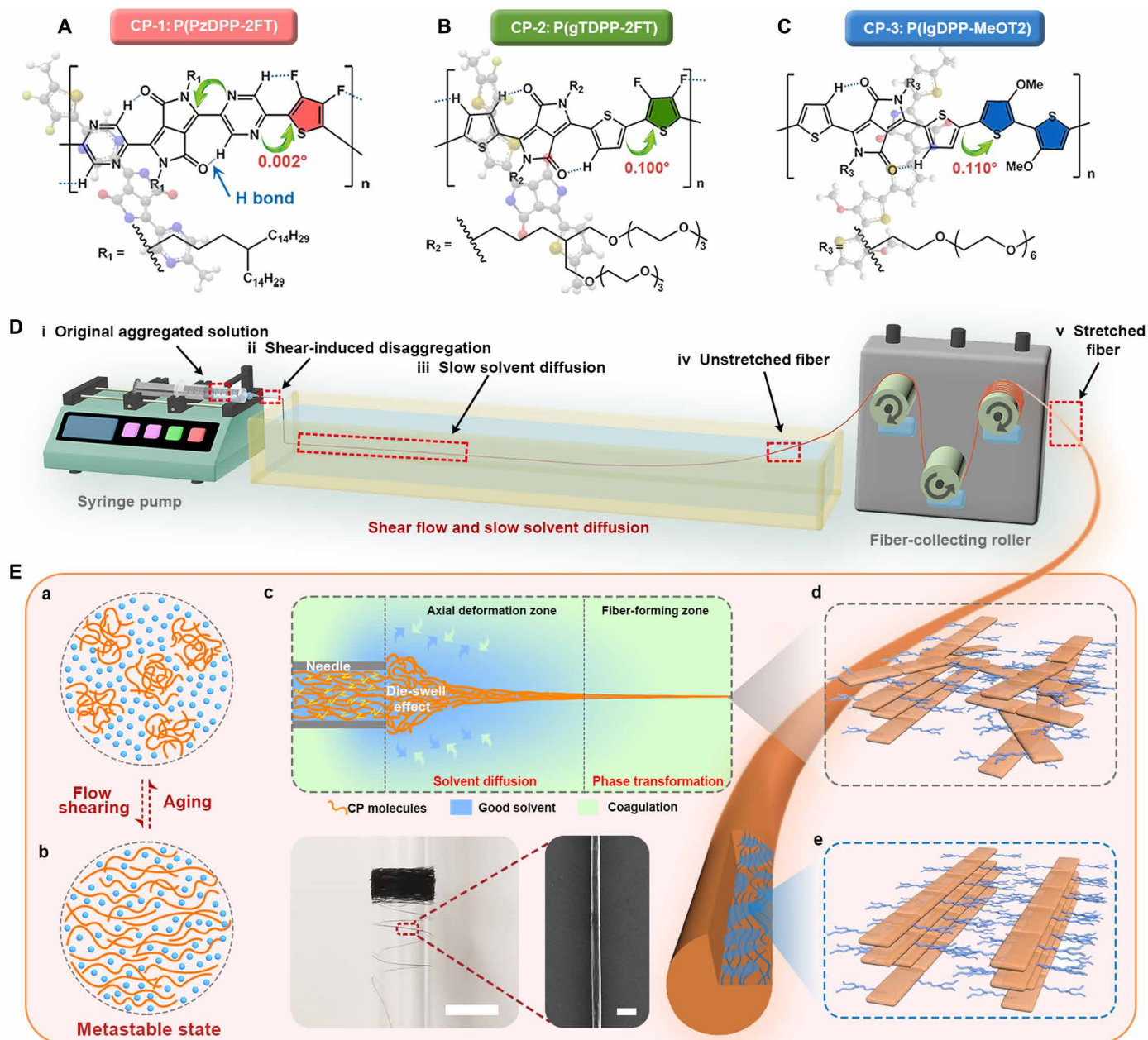


Fig. 1. Polymer chemical structures and schematic illustration of the mechanism of the FLEX method. Chemical structures of the polymers: (A) P(PzDPP-2FT) (CP-1), (B) P(gTDPP-2FT) (CP-2), and (C) P(lgDPP-MeOT2) (CP-3). (D) Schematic of the experimental setup and the major components for the homemade continuous wet-spinning apparatus and continuous production of semiconducting polymer fibers. (E) Schematic illustration of the flow-enhanced crystallization (FLEX) mechanism: (a) original aggregated polymers inside the syringe, (b) solution flow disaggregates and aligns the semiconducting polymers in the needle; (c) slow solvent diffusion and exchange in the coagulation bath can lead to enhanced crystallinity; (d) before and (e) after drawing/stretching. The insets are the photograph (scale bar, 1 cm) and SEM image (scale bar, 20 μm) of CP-1 fibers obtained through continuous production and collection. The CP-1 semiconducting fibers showed an average diameter of $9.77 \pm 0.73 \mu\text{m}$ (figs. S2 and S3).

with superior electronic performance as stretchable conductors, OTEs, OECTs, and biosensors.

RESULTS

Discovery of flow-induced polymer disaggregation and alignment

Three distinct CPs are used in this study (Fig. 1, A to C, fig. S4, and table S1). Two of them, namely, P(PzDPP-2FT) (CP-1) (25) and P(gTDPP-2FT) (CP-2) (26), belong to the acceptor-acceptor (A-A)-type n-type polymer category. The third polymer, P(lgDPP-MeOT2) (CP-3) (27), falls under the donor-acceptor (D-A)-type p-type polymer category. CP-1 contains hydrophobic alkyl side chains, while CP-2 and CP-3 have hydrophilic ethylene glycol side chains. All these polymers exhibited excellent charge transport properties due to their highly planar backbones with intramolecular non-covalent interactions (fig. S5 and Discussion) and strong interchain π - π stacking interactions.

Initial failed attempts indicate that the conventional high-concentration wet-spinning approach is unsuitable for continuously producing high-performance semiconducting polymer fibers because they usually have limited solubility and are strongly disorderly aggregated in solution (28). We hypothesize that the key challenge in addressing the spinning hurdles of semiconducting polymers is finding ways to disentangle and align polymer chains in solution (Fig. 2A). Thus, we reduced the concentration of the polymer solution to 10 mg ml^{-1} and used small-diameter and long needles to generate strong strain rates to disaggregate the entangled polymer chains and align them along the flow direction. The spinning concentration of 10 mg ml^{-1} is above the critical overlap concentration (c^* , 2.5 mg ml^{-1}) (fig. S6 and Discussion) (29, 30). Extremely, we can achieve spinning at the lowest concentration of $\sim 2 \text{ mg ml}^{-1}$ (fig. S7 and table S2). The polymer solution exhibited obvious shear-thinning behavior, indicating polymer disaggregation or alignment at increasing shear rates (fig. S6A) (31). Furthermore, we simulated the solution flowing inside the needles and found that both extensional flow and shear flow contribute to the disaggregation and alignment of polymer chains (figs. S8 and S9 and Discussion) (32, 33).

The ultraviolet (UV)-visible (vis)-near-infrared (NIR) absorption spectra demonstrate that, as the flow speed increased, the absorption peak at $\sim 720 \text{ nm}$ decreased, which is probably due to the polymer disaggregation (Fig. 2, B and C, and fig. S10, A and B). Once the critical injection speed of 0.04 ml min^{-1} was exceeded, there was a sharp decline of the peak, indicating a notable disaggregation, which matched well with our simulation results (Fig. 2C, fig. 9C, and Discussion). To determine whether the disaggregation belongs to breaking down larger aggregates into smaller ones or dissolving aggregates into single polymer chains, we conducted dynamic light scattering (DLS) photoluminescence (PL) measurements. DLS confirmed such flow-induced disaggregation effect, and the polymer aggregates' size decreased from 50 to $<5 \text{ nm}$ (fig. S10, C and D). The PL spectra also supported the disaggregation, where we observed decreased emission from the aggregated phase and increased emission from single polymer chains (Fig. 2K, fig. S11, and Discussion). These results well corroborate our hypothesis of flow-induced disaggregation, which breaks down the larger aggregates into smaller ones while further dissolving the aggregates into single polymer chains also seems possible. This disaggregated state is kinetically metastable

because the disaggregated polymers could reaggregate after several days of aging (Fig. 2D).

The geometric size of the spinning needle determines the strain rates of polymers (fig. S9B), which influences the crystallinity and polymer chain alignment of the fibers. We prepared CP-1 fibers with a coagulation solvent ethanol (EtOH) using needles with different diameters (D) and lengths (L) and compared their microstructures using wide-angle x-ray scattering (WAXS). Decreasing the needle diameter or increasing the needle length greatly enhanced the alignment of polymer chains in the fibers (Fig. 2, E and F), compared to spin-coated films (fig. S12). As the needle diameter decreases or length increases, EtOH fibers exhibited a noteworthy rise in Herman's orientation factor (f) (34) from 0.42 to 0.74 , decreased lamellar distances from 27.2 to 25.9 \AA , and strengthened π - π stacking diffraction peaks (3.54 \AA), indicating much better chain alignment and increased crystallinity (fig. S13, A and B). Another crystallization peak at 1.62 \AA^{-1} (3.85 \AA) appeared, which has not been observed in the polymer films (Fig. 2G). We ruled out the possible attribution of the ordering along polymer backbone through WAXS analysis and molecular modeling (fig. S14 and Discussion). We attributed this additional peak to the orderly arrangement of the alkyl side chains, as well-ordered side chains usually have a d -spacing within 3.6 to 4.0 \AA (35, 36). To support this, we used differential scanning calorimetry (DSC) measurements and molecular dynamic (MD) simulations (figs. S15 and S16 and Discussion). Compared with polymer solids and fibers with lower or without side-chain crystallinity, fibers with better crystallinity showed higher side-chain melting points (fig. S15). Previous studies have shown that higher alkyl chain melting points indicate better alkyl chain packing order and crystallinity in solid state (37). MD simulations also support the good interdigitation of the long alkyl side chains. In addition, the WAXS of CP-2 and CP-3 fibers did not show such peaks using FLEX because of their ethylene glycol side chains, which also supports the attribution of this peak to the ordered packing of the alkyl side chain in CP-1 fibers (fig. S17). We also calculated the coherence length (L_c) (38) and paracrystalline disorder (g factor) (39) of the fibers. Fibers fabricated using thinner and longer needles showed notably increased L_c and decreased g factors (fig. S18, C and D, and table S3). When using a shear flow to disentangle the polymer in solution, followed by thin film spin-coating, we observed redshifted and enhanced 0-0 absorption peaks and a distinct aggregation peak at 825 nm (Fig. 2H) (40). This demonstrates that disentangled polymer chains result in improved crystallinity even for thin film fabrication. Flow-induced crystallization has been reported in conventional polymers during processing (41). In these polymers, increasing spinning solution concentration is a common strategy to enhance molecular entanglement to meet spinning requirements. However, it is not suitable for CPs. Decreasing concentration and disentangling polymer in solution is essential for our FLEX method, which is not necessary for conventional polymers.

Antisolvent flow-controlled polymer crystallization

In traditional wet-spinning processes, antisolvents are commonly used to induce polymer precipitation. Apart from this effect, we will demonstrate that choosing antisolvents is crucial for regulating the crystallinity and chain alignment of semiconducting polymer fibers (Fig. 2I). We observed that the CP-1 microfiber's crystallization behavior is highly influenced by the antisolvent polarity (fig. S18A and table S4). No matter the needle size, increasing antisolvent polarity

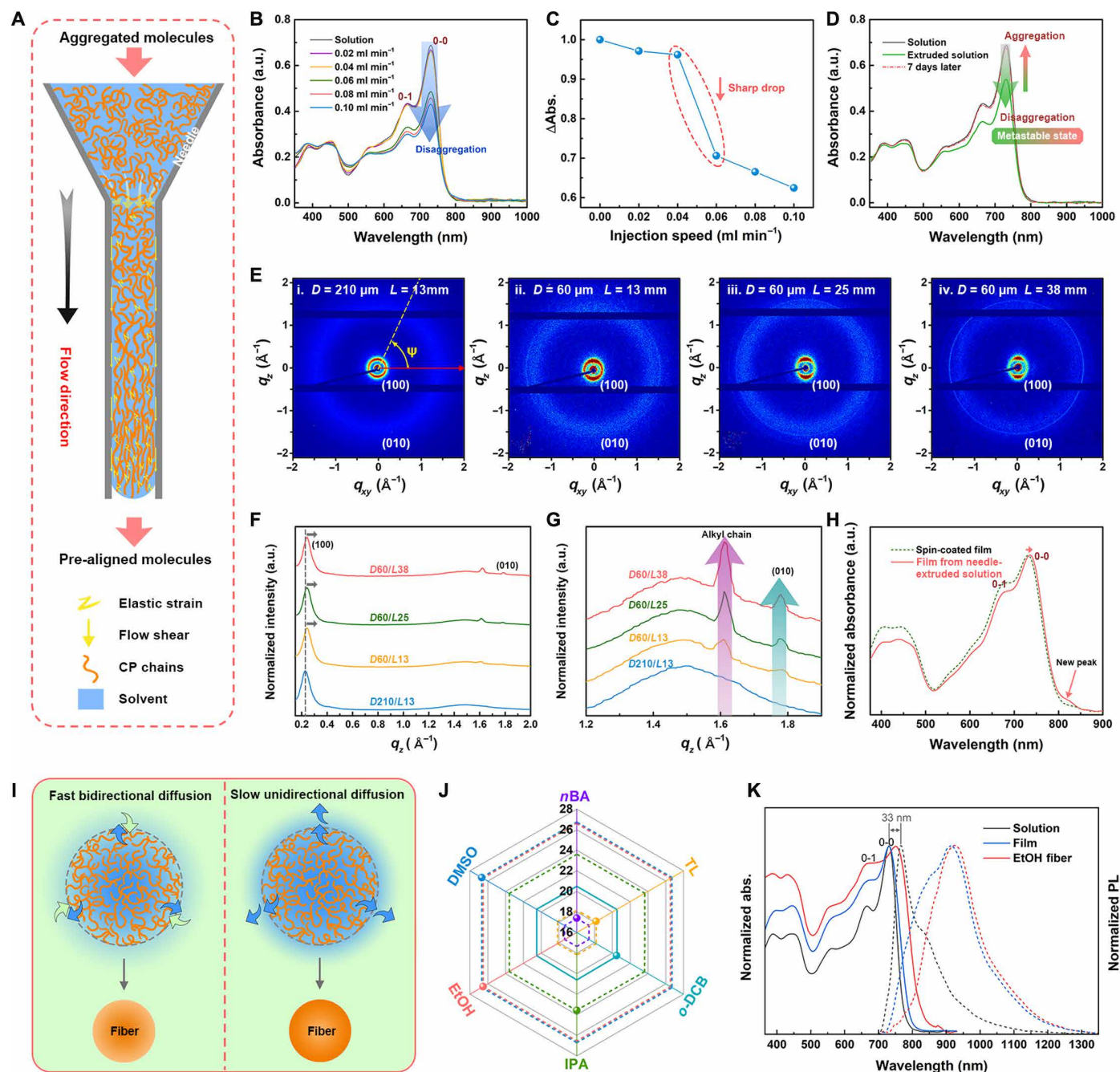


Fig. 2. Effects of shear flow-induced polymer disaggregation and alignment. (A) Scheme of the FLEX mechanism inside the spinning needle: Flow shear disaggregates the CP molecules. (B) Absorption spectra of CP-1 solution before and after being extruded at various injection speeds (0.02, 0.04, 0.06, 0.08, and 0.1 ml min⁻¹). a.u., absorbance units. (C) Relative changes of the intensity at ~720-nm absorption peaks after being extruded at different flow velocities. (D) Absorption spectra of CP-1 solution before and after 60-μm needle extruding and followed by aging for 36 hours. (E) 2D-WAXS patterns of wet-spun semiconducting microfibers using needles with different inner diameters: 210 μm (D210), corresponding to a central velocity of 17 mm s⁻¹ and 60 μm (D60), central velocity of 215 mm s⁻¹ and with different lengths: 13 mm (L13), corresponding to a shear time of 0.06 s, 25 mm (L25, shear time of 0.12 s), and 38 mm (L38, shear time of 0.18 s). The red arrow indicates the fiber direction. (F) Line profiles of the integrated intensity (normalized to the maximum intensity) versus q value extracted from the 2D WAXS patterns. (G) Enlarged line profiles with q values from 1.0 to 1.9 Å⁻¹, showing obvious changes of the π - π and alkyl chain diffraction peaks. (H) Comparison of the absorption spectra of the directly spin-coated film and the film spin-coated from a CP-1 solution extruded through a D60/L38 needle. (I) Schematic illustration of the solvent diffusion patterns for the fast bidirectional diffusion and slow unidirectional diffusion according to Hansen's principle. (J) Comparison of the total Hansen solubility parameters (HSPs) of the solvent (σ -DCB) and the antisolvents [toluene (TL), *n*-butyl acetate (*n*BA), isopropyl alcohol (IPA), ethanol (EtOH), and dimethyl sulfoxide (DMSO)]. (K) Comparison of the normalized absorption (abs.) spectra (solid lines) and the normalized photoluminescence (PL) spectra (dash lines) ($\lambda_{ex} = 470$ nm) of the CP-1 solution, spin-coated film, and the microfiber wet-spun in EtOH.

leads to a monotonic decrease in chain alignment (fig. S18, A, E, and F), while an increase in the π - π stacking and side-chain crystalline (fig. S18B). Using more polar antisolvents always leads to increased crystallinity but decreased alignment. Fibers from more polar antisolvents show a notable increase in L_c and decrease in g factors (fig. S18, C and D). Specifically, g factor decreased from 16.5 to 4.2%, comparable to the highly crystalline poly(3-hexylthiophene-2,5-diyl) (P3HT) films (42). The absorption further confirmed the high crystallinity of the fibers from more polar solvents, with toluene (TL) fibers showing a blueshift compared to the film and EtOH fibers showing a redshift (fig. S19 and Discussion). In addition, the EtOH fiber showed pronounced a redshift and narrowing emission peak, indicating the formation of highly ordered aggregates (Fig. 2K). From combined absorption spectra and PL spectra, we think that the polymer might adopt a more planar backbone conformation or different interchain packing in EtOH fiber, which is further supported by time-dependent density functional theory (DFT) calculations (fig. S20 and Discussion).

We propose that such antisolvent-dependent behavior relates to the antisolvent diffusion process during coagulation, which can be explained by the Hansen solubility parameters (Fig. 2J and fig. S21) (43). Hansen's solubility theory characterizes the miscibility of a solvent-nonsolvent pair using their relative energy difference ($\Delta\delta$), which determines the solvent diffusion mode and crystallization rate (fig. S21B). When $\Delta\delta$ between two solvents, such as TL and *o*-DCB, is close, they are highly miscible, leading to a fast bidirectional diffusion (Fig. 2I). When $\Delta\delta$ is largely different (e.g., EtOH versus *o*-DCB), they have poor miscibility, causing slow unidirectional diffusion (44). The latter leads to a slower phase transition and crystallization than the former, resulting in fibers with higher crystallinity but less alignment (polymers aligned by the extensional and shear flow can relax to random orientation). The slow solvent diffusion and crystallization process is also supported by our colored solution tracing experiment (fig. S22, Discussion, and movie S2). We did not observe strong π - π stacking and alkyl side-chain crystalline peaks in TL microfiber, which exist in EtOH fibers (fig. S18A, G and H), further demonstrating the critical importance of both the flow inside the needle and the antisolvent diffusion in the coagulation bath.

Further enhancing fiber's mechanical properties by stretching

We chose EtOH as the antisolvent, because dimethyl sulfoxide has high boiling point and results in solvent residue in fibers, further leading to poor mechanical properties and failure in continuous production. We found a positive correlation between the mechanical properties and the crystallinity of the fibers (fig. S23 and Discussion) (38). For example, microfibers produced with EtOH showed a high tensile strength of ~ 90 MPa and stain-to-failure of $\sim 35\%$, much better than the TL fibers (Fig. 3A). We performed a cyclic stretch-rebound test with a strain of 10% for CP-1 fibers, indicating that the semiconducting fiber is not fully elastic and can be plastically stretched (fig. S24). The excellent mechanical properties allow us to post-stretch the fibers. The 10% stretched EtOH fibers displayed even better mechanical properties with high tensile strength (>200 MPa), toughness (>80 MJ m $^{-3}$), and enhanced strain-to-failure $>50\%$ (fig. S1, A and B). These values, to our knowledge, are already comparable or superior to many synthetic fibers and are the record values in semiconducting polymer fibers and films (Fig. 3, B and C). Notably, this strong fiber also has a low density (0.96 g cm $^{-3}$), comparable to the

lightest synthetic fiber polypropylene (fig. S25). We observed reduced lamellar distance, enhanced L_c , reduced g factors, and enhanced alignment after stretching, suggesting that polymer chains tend to arrange more compactly and ordered (Fig. 3, D and E, fig. S26, and table S5). When the fiber was stretched from 0 to 50%, the orientation factor (f) of the fibers increased from 0.67 to 0.91. Thus, the strengthening and toughening after stretching is probably due to the slow stretching-induced orientation and enhanced crystallinity (45). Using FLEX, we also obtained CP-2 and CP-3 fibers, exhibiting exceptional mechanical properties with tensile strengths of >100 MPa and toughness of >20 MJ m $^{-3}$ (fig. S27).

Good mechanical properties in traditional synthetic fibers usually necessitate strong interchain interactions. For example, nylon and polyimide fibers contain interchain hydrogen bonds. However, CPs tend to form lamellar packing with side chains situated between the lamellae, resulting in weak interactions and inferior mechanical properties. In our study, we credit the outstanding mechanical properties to the disaggregation of polymers from larger aggregates into smaller ones, which leads to better backbone alignment and side-chain crystallization and thereby contributes to the high stretchability of CP-1 fibers (fig. S28). The ordered arrangement and crystallization of alkyl side chains can increase inter-lamellae interactions and enhance fiber strength (46). This type of well-organized side-chain packing has rarely been achieved in literature (47). Recent studies have suggested that ordered alkyl side-chain packing could greatly improve the mechanical strength of CP films (48, 49). We also performed transmission electron microscopy and small-angle x-ray scattering (SAXS) to confirm the fibers' microstructures to exclude other possible mechanisms (fig. S29 and Discussion).

CP-1 fibers can be easily bent and knotted with a radius of curvature of <5 μm , a record-low value compared to other semiconducting fibrous materials (Fig. 3F and fig. S30, A to C) (3, 50–52). Moreover, the fibers show an effective bending stiffness of 0.7 to 1.3 nN-m, comparable to that of neural tissues (53, 54). These attributes make them ideal for use in implantable bioelectronics, such as brain-computer interfaces (5, 19). Figure 3G presents a radar diagram that quantitatively compares important parameters of fibrous materials, and our semiconducting fibers excel in all these parameters. Their mechanical properties also enable them to be directly integrated with textiles through threading and sewing (Fig. 3H). By embedding these stretchable fibers into polydimethylsiloxane elastomers, devices with excellent resilience could be prepared (fig. S30, D and E), suggesting their potential applications in elastic electronics (23, 55).

Strain-enhanced electronic performance for fiber electronics

Wearable electronics typically undergo substantial deformation under bending, twisting, and folding conditions, causing mechanical damage and leading to electrical failure (56). Therefore, stretchable electronics that conform to human skin and withstand mechanical deformation have sparked growing interest (5, 19, 57). The excellent mechanical properties and biocompatibility (fig. S31 and Discussion) of the fibers encouraged us to explore their potential applications (Fig. 4A). Because of the high strength of the semiconducting fibers, they can be easily used for sewing without breaking (fig. S32A and Fig. 3H).

After doping, the CP-1 fiber can function as a high-performance n-type conductor (Fig. 4, B and C, and fig. S32B). It shows unique strain-enhanced electrical conductivities. The CP-1 fiber showed a decreased resistance of more than 20% after stretching to 50%,

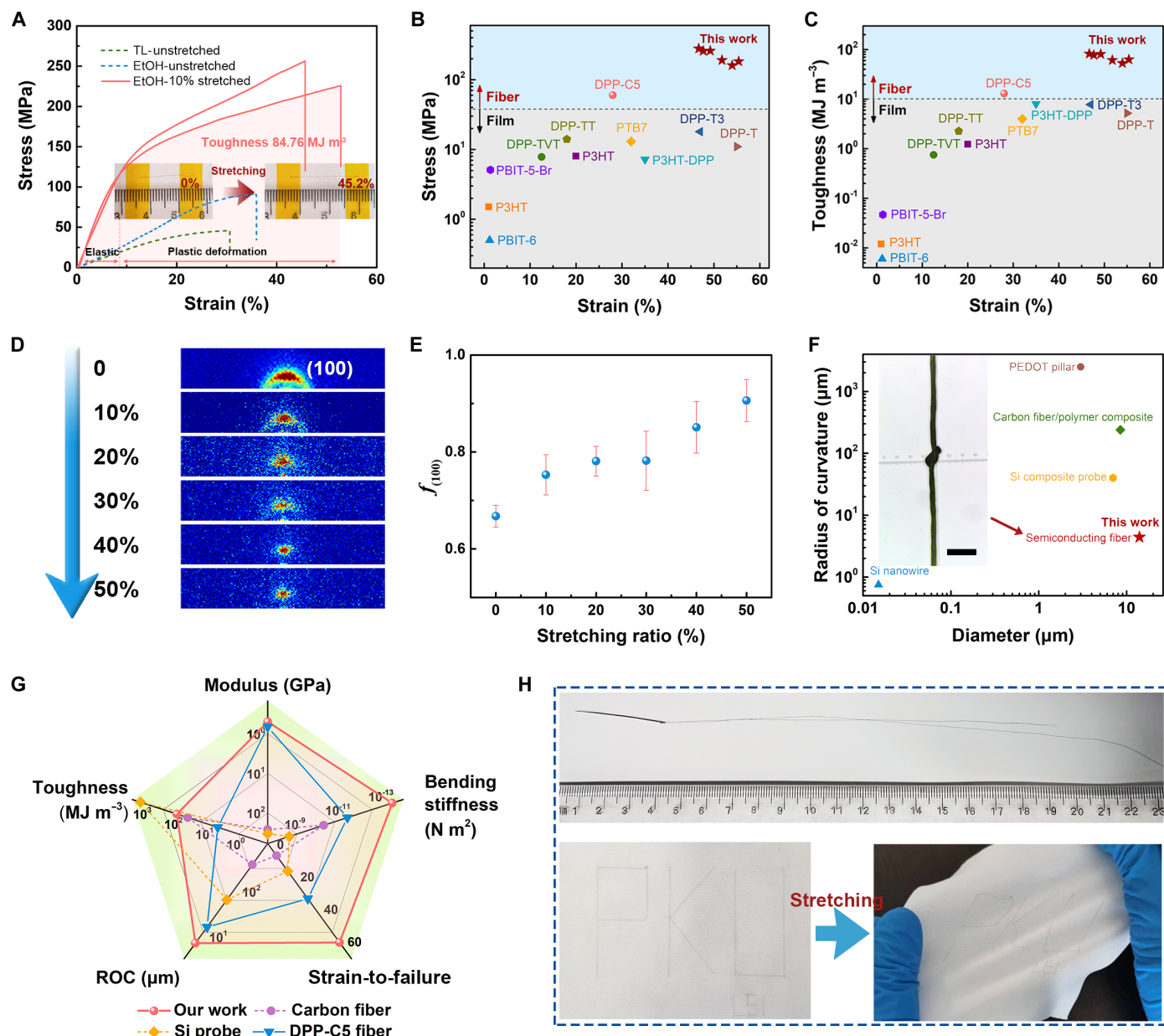


Fig. 3. Mechanical properties, stretching enhanced alignment, and integration ability of the fibers. (A) Stress-strain curves of the undrawn TL fiber, undrawn EtOH fiber, and two drawn EtOH fibers. Comparison of the (B) tensile strength and (C) toughness versus breaking strain of our semiconducting polymer fibers with those of other CP films and fibers reported in the literature (69–72). (D) 2D-WAXS patterns and (E) the calculated f factor of the (100) reflection of CP-1 fibers with different stretching ratios. (F) Comparison of the radius of curvature (ROC) for our fibers with other reported fibers/probes that have been used in electrophysiological interfaces. Inset is an optical micrograph showing a knotted fiber with a ROC of less than 5 μm . Scar bar, 50 μm . (G) Comparison of several key mechanical properties among several fibrous materials: carbon fiber, Si probe, DPP-C5 fiber, and our CP-1 fiber. (H) Photographic image of a “PKU” logo sewed on a non-woven fabric, demonstrating the good threading and sewing ability of our fibers. After integration with fabrics, the fibers show excellent stretchability.

equivalent to a conductivity increase from 76 to 173 S cm^{-1} after considering the geometric change. To the best of our knowledge, such an intrinsically strain-reduced resistance phenomenon has rarely been observed before (Fig. 4B), and the conductivity of 173 S cm^{-1} is also a record value for n-doped semiconducting polymers (fig. S33) (25, 58). We ruled out the ionic contributions to the electrical conductivity of CP-1 fibers, which is a typical electronic conductor (fig. S34 and Discussion).

A wearable electronic system typically includes sensors, power sources, and processors. As a proof of concept, CP-1 fiber OTEs were fabricated (Fig. 4D), which could potentially serve as a power source. The thermoelectric performance of n-doped CP-1 fibers are closely related to their fabrication and doping methods (fig. S35). Higher thermoelectric performance can be achieved with higher fiber crystallinity and certain strain. At 30% strain, we achieved a high n-type conductivity of 149 S cm^{-1} , a Seebeck coefficient of $-98 \mu\text{V K}^{-1}$, and

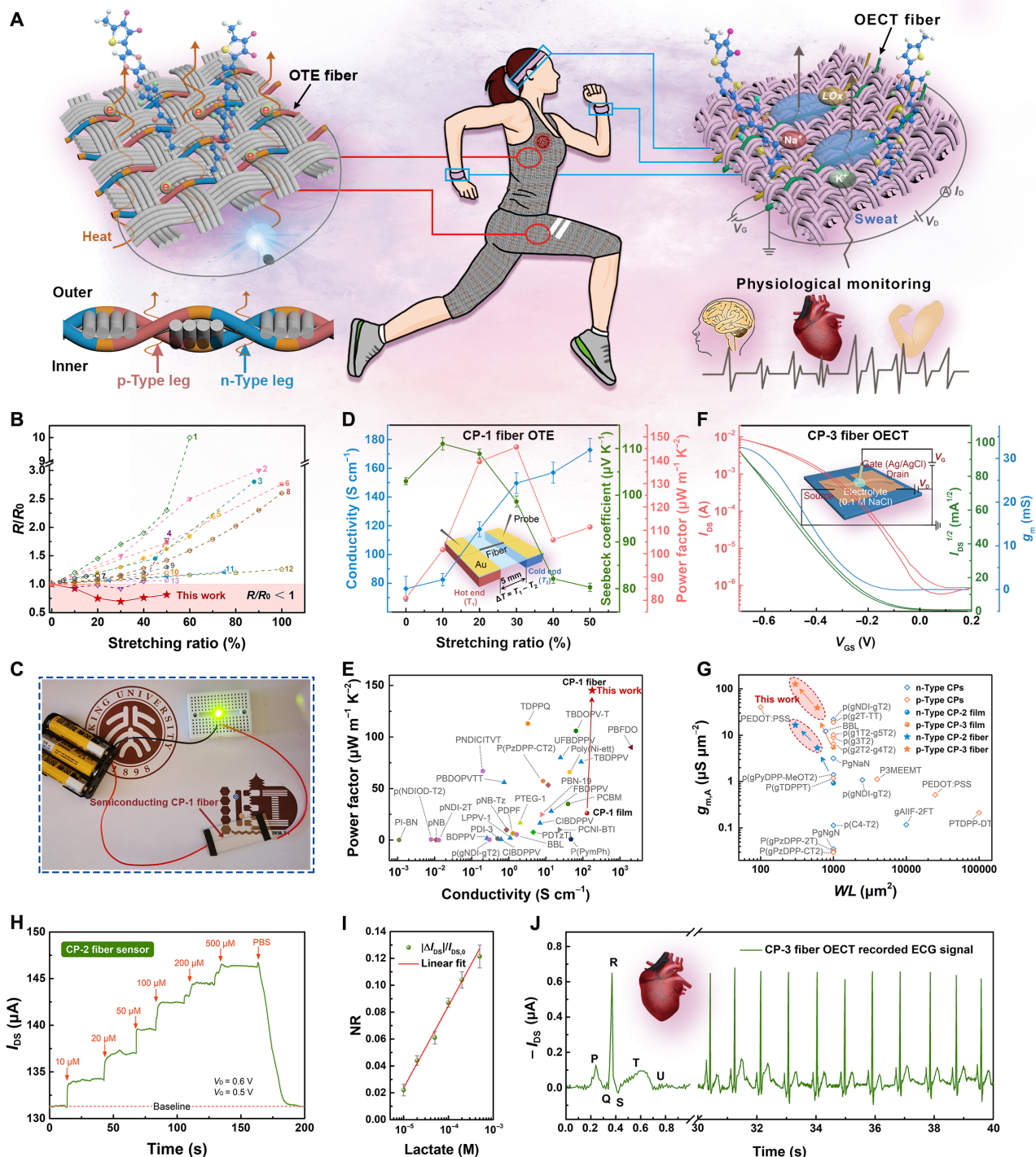


Fig. 4. Wearable electronic applications of the fibers produced with FLEX. (A) Schematic diagram of potential wearable applications of the semiconducting polymer fibers. (B) Relative resistance (R/R_0) over strain plots showing decreased resistance under strain for CP-1 fiber versus literature-reported stretchable electronics. All previously reported structures suffer from severe resistance ascent from stretching (detailed data and references are in table S6). (C) Photograph of a lighted light-emitting diode that was connected by an n-doped CP-1 fiber as the conductor. (D) Dependence of geometric corrected electrical conductivities, Seebeck coefficients, and PFs of CP-1 fibers at various stretching ratios (0, 10, 20, 30, 40, and 50%). Inset is a cartoon illustration of the architecture of the fiber OTE device measurement setup. The error bars represent the SDs. (E) Comparison of PFs vs. conductivity for CP-1 fibers and other reported n-type polymer TE materials. (F) Representative p-type transfer characteristic and corresponding g_m curves of a CP-3 fiber OECT ($W/L = 15\ \mu m/20\ \mu m$). (G) Comparison of the $g_{m,A}$ values of currently reported OECT devices. The data of the summarized OECT performances are listed in table S7. (H) Real-time response of the CP-2 fiber OECT (source-drain current, I_{DS} , as a function of time) as successive amounts of lactate are added to the PBS solution containing the lactate oxidation enzyme (LOx). (I) Normalized calibration curves derived from the chronoamperometric response of the CP-2 fiber OECTs. (J) Real-time recorded ECG signals from CP-3 fiber OECTs.

a power factor (PF) of $146 \mu\text{W m}^{-1} \text{K}^{-2}$ (Fig. 4D). The PF value is among the highest in n-type polymer thermoelectrics, substantially surpassing that of the CP-1 film (Fig. 4E). The substantial enhancement of the conductivity and Seebeck coefficient is probably due to the improved crystallinity and chain alignment in the fiber.

OECTs are attractive for bioelectronics and biosensors due to their good biocompatibility, low operation voltage, and high transconductance (59). For many applications, such as single-neuron sensing, the area of the OECT needs to be the smaller, the better. To evaluate the performance of a transistor-based sensor, transconductance (g_m) is often used. After considering the transistor area (W by L), the area-normalized transconductance [$g_{m,A} = g_m/(WL)$] is used for device performance comparison (60). Both CP-2 and CP-3 fiber OECTs demonstrate extraordinary performances among all n- and p-type OECTs (Fig. 4, F and G, and fig. S36). The $g_{m,A}$ values as high as 16 and $127 \mu\text{S } \mu\text{m}^{-2}$ are achieved for n-type CP-2 and p-type CP-3 fibers, respectively. These values are about 18 times and 24 times greater than those of their film devices. The CP-3 fiber OECTs exhibit the highest $g_{m,A}$ values among all planar OECTs, even comparable to recently developed vertical OECTs (60).

On the basis of these fiber OECTs, we successfully developed lactate and electrocardiogram (ECG) sensors (Fig. 4, H to J, and fig. S37) (61). The CP-2 and CP-3 fiber sensors exhibited excellent linearity within the range of 10 to $500 \mu\text{M}$, demonstrating high sensitivity of 2.01 and $9.37 \text{ mA mM}^{-1} \text{ cm}^{-2}$, respectively. These sensitivities are among the highest in recently reported lactate sensors (fig. S32H) (62–65). Besides, the sensors show good selectivity and accuracy (fig. S38). We also used these fiber OECTs to record ECG signals, observing remarkable signal-to-noise ratios of 39 and 54 for CP-2 and CP-3 fiber OECTs, respectively (Fig. 4J and fig. S37, G to I). Therefore, our CP fibers exhibit great potential for integration into wearable electronics for health monitoring.

DISCUSSION

Unlike the traditional wet-spinning approach that requires a highly concentrated polymer solution to meet good spinnability, we oppositely lower the polymers' solution concentration to achieve the continuous fabrication of the CP fibers. The key factor in addressing the spinning hurdles of semiconducting polymers is to disentangle and align polymer chains by extensional and shear flow and control the fiber crystallinity by solvent/antisolvent diffusion flow. The resulting fibers displayed remarkable mechanical properties and interesting strain-enhanced electronic performance that have rarely been achieved. Previous studies in CPs mostly focused on thin-film devices. This work demonstrates that the electronic performance of well-engineered fibers could surpass those of thin films due to enhanced polymer chain alignment and crystallinity. We anticipate that the FLEX method, along with the fluid mechanical effects uncovered in this work, will serve as a universal approach and framework for the scalable production and creation of tough and durable semiconducting fibers for wearable electronics and bioelectronics.

MATERIALS AND METHODS

Materials

CPs (CP-1, CP-2, and CP-3) were synthesized as previously described (25–27). An aqueous dispersion of PEDOT:PSS (Clevios PH1000; solid content of 1.1 to 1.3 wt %) was purchased from

Heraeus. Lactate oxidase (LOx; solid content of ≥ 20 units/mg) was purchased from Beijing MREDA Technology Co., Ltd. Phosphate-buffered saline (PBS; 0.01 M, pH 7.2 to 7.4) was purchased from Alfa Aesar. Ethylene glycol, dodecyl benzene sulfonic acid, and (3-glycidyloxypropyl)trimethoxysilane were purchased from Sigma-Aldrich. All solvents used were purchased from Sigma-Aldrich. Silver slurry (MCN-ED002) was purchased from MECHANIC. Rhodamine B (AR) was purchased from Beijing Qisong Biotechnology Co. Ltd. Tetrakis(dimethylamino)ethylene (TDAE) and 1-butyl-3-methylimidazolium bis(trifluoromethylsulfonyl)imide (BMI-TSFI) were purchased from MREDA. All of the chemicals and materials were used without further purification after purchase.

Fabrication of CP fibers

First, the CPs (CP-1, CP-2, and CP-3) were fully dispersed in good solvents [1,2-dichlorobenzene (*o*-DCB)] at 120°C and were filtered through a $0.45\text{-}\mu\text{m}$ polyvinylidene difluoride filter as the spinning solution. Subsequently, the spinning solution was fed into a 2-ml syringe with a stainless-steel blunt needle with different diameters (210, 160, 110, and $60 \mu\text{m}$) and lengths (13, 25, and 38 mm). The syringe was then mounted to a custom-made wet-spinning apparatus with a syringe pump (LSP02-1BY), a polytetrafluoroethylene (PTFE) coagulation bath, and fiber collection rollers. The spinning dope was extruded through spinning needles with a rate ranging from 0.02 to 0.14 ml min^{-1} into different coagulations. Antisolvents with different polarities were used as the coagulation baths. Note, because of the substantial differences in the molecular structure of different conjugated copolymers, the applicable polymer-solvent-nonsolvent triads for wet-spinning are also various (table S3). CP fibers were directly drawn out from the coagulation bath and wound with a roller at a collecting speed of 0.5 to 1 m min^{-1} , and the speed of the last roller increased by 10% to achieve fiber stretching and mechanical enhancement.

Characterization of spinning solutions and wet-spun microfibers

Absorption spectra were recorded on PerkinElmer Lambda 750 UV-vis spectrometer. PL spectra were conducted on a Steady State and Transient State Fluorescence Spectrometer (FS980, Edinburgh, UK). The wavelength of the excitation light is 470 nm . The excitation grating width and emission grating width are both 10 nm . DLS was performed using a Zetasizer Nano ZS90 (Malvern Instruments). The dimensions and morphologies of the microfibers were characterized using field-emission scanning electron microscopy (S4800, Hitachi, Japan) at 10 kV and $10 \mu\text{A}$ without Pt sputtering. The rheological properties of the polymer solution were measured using a rheometer (MCR 301, Anton Paar, Austria) under steady shear conditions.

WAXS and SAXS measurements were performed in transmission mode using the Ganesha system. The source was GeniX3D Cu ULD 8 keV with a wavelength of 1.54189 \AA . Typically, CP microfibers were cut and aligned into a bundle and placed in an aperture card. The aperture card with the aligned fiber bundle was then transferred to the WAXS sample holder and placed at 101.17 mm from the 2D detector (Dectris Pilatus 200 K). Exposure time was 600 s . Data processing to obtain the integrated diffracted intensity versus q and azimuthal angle, Ψ , was performed using the software Foxtrot provided by Ganesha. DSC analyses were performed on a TA Instruments Q2000 analyzer.

The tensile properties of the CP fibers were measured using a Shimadzu EZ-LX at a strain rate of $1\% \text{ min}^{-1}$. Samples were mounted on aperture cards (1-cm-length window) with commercial epoxy resin and allowed to air dry. The stress-strain curves were recorded directly, and Young's modulus and toughness were calculated accordingly.

MD calculations

On the basis of the quantum-chemical calculations, a force field derived from the Dreiding force field was used, in which the torsion potentials between adjacent conjugated units have been reparameterized against $\omega\text{B97X-D/6-311G(d,p)}$ calculation. DFT-optimized geometries of the 3435 dimers were used as initial structures, and atomic charges were resigned according to DFT-calculated restrained electrostatic potential (RESP) charges. We used the methodologies according to the literature to simulate the crystalline and disorder region of CP-1 P(PzDPP-2FT). All MD simulations were performed using Material Studio (66), and all DFT calculations were performed with Gaussian 16 package (67).

Cell culture experiments

The sample substrate was preloaded into a six-well plate. Mouse fibroblasts (L929; 5×10^5) were seeded into each well and cultured in high-glucose Dulbecco's modified Eagle's medium with 10% fetal bovine serum (6021031, DAKWE), penicillin (100 U/ml; Invitrogen), and streptomycin (100 U/ml; Invitrogen) at 37°C with 5% CO_2 and 95% humidity. After 24 hours, live/dead staining (catalog no. 40747ES76, Yeasen) was performed to evaluate the biocompatibility of the substrates. Briefly, cells were thoroughly washed with $1\times$ assay buffer, and the staining working solution was prepared by adding $5 \mu\text{l}$ of calcein-AM solution (2 mM) and $15 \mu\text{l}$ of propidium iodide solution (1.5 mM) to 5 ml of $1\times$ assay buffer and mixing thoroughly. Staining working solution ($100 \mu\text{l}$) was added to $200 \mu\text{l}$ of cell suspension, mixed, and incubated at 37°C for 15 min. Live cells (green fluorescence) and dead cells (red fluorescence) using a $490 \pm 10\text{-nm}$ excitation filter under a fluorescence microscope (Nikon DS-F).

CP fiber OTE device fabrication and electrical property measurements

To fabricate the fiber OTE devices, the wet-spun CP-1 microfibers were laid flat onto the cleaned glass substrates (2.54 cm by 2.54 cm), followed by evaporating 50-nm Au on glass using a stainless-steel shadow mask to define the channel area with a length of 5 mm. Then, the glass substrates loaded with microfibers were transferred into a glove box to n-dope with different methods.

The thermoelectric properties were studied in a nitrogen glove box to avoid temperature fluctuation and O_2 /water dedoping. TDAE was used to dope CP-1 microfibers due to its strong n-doping ability. The fumigation method was achieved by enclosing the glass substrates in a TDAE atmosphere for different times. After different exposure times in TDAE vapor, the glass substrates were put on the probe stage to measure the conductivity or on a Seebeck stage with a hot end and a cold end to record the Seebeck curves. The conductivity was collected by two-probe measurements in a nitrogen glove box with a Keysight B1500A semiconductor parameter analyzer or sourcemeters (Keithley 2636B and 2182A). TLM method was used to eliminate the interference of contact resistance. Because the four-probe method will amplify the uneven structure along the length

direction, resulting in a notably larger test resistance. Twenty devices were measured for each data point. The Seebeck coefficients (S) can be calculated from the Seebeck curve by the formula $S = \Delta V / \Delta T$. ΔV is the thermal voltage between the hot and cold ends of the device at a temperature gradient ΔT , the ΔV was monitored by a Keysight B1500A semiconductor parameter analyzer or sourcemeters (Keithley 2636B and 2182A), and the temperature difference was introduced by Joule heating (heater) and condensate water cooling system. To accurately figure out the temperature difference ΔT between the two contact pads, two temperature sensing wires (5-nm Cr/20-nm Au bilayer) were introduced on the hot and cold ends of the Seebeck stage. The other doping method, ion exchange, required mixing TDAE with different ratios and 5% (w/v) ionic solution BMI-TSFI in corresponding coagulation solution, which was used as dopants to immerse devices for 1 s followed by the above measurements.

CP fiber OECT fabrication and performance measurements

A silicon wafer with a 300-nm-thick SiO_2 layer was used as the substrate. It was ultrasonically cleaned in acetone, deionized water, and isopropyl alcohol, followed by nitrogen blow drying and then with oxygen plasma treatment for 5 min. The CP fibers were set up on the substrate relying on Coulombic force. Next, 50 nm of Au was deposited by thermal evaporation using a stainless-steel shadow mask as the electrodes. Here, the patterned Au source-drain electrodes defined the channel dimensions of W (fiber diameter) and L (width of the shadow mask). At last, a droplet ($\sim 20 \mu\text{l}$) of NaCl solution (0.1 M) was applied onto the electrode overlapping area, and an Ag/AgCl electrode (Warner Instruments) was inserted in the droplet acting as the OECT gate electrode. The device characterization was performed on a probe station using a Keithley 4200 SCS analyzer or an Fs-Pro semiconductor parameter analyzer, PDA.

CP fiber sensor device fabrication and characterization

The fiber OECT devices were fabricated as the above method. The active material, PEDOT:PSS solution [19 ml of Clevis PH1000, 1 ml of ethylene glycol, $50 \mu\text{l}$ of dodecyl benzene sulfonic acid, 1 wt % (3-glycidylxypropyl)trimethoxysilane] was drop cast on Au-coated substrate and hard-baked (125°C , 60 min) to generate a homogeneous film.

For the sensing experiments, LOx in the PBS (10 mg ml^{-1}) was drop cast on the device active area (channel and gate) and soaked overnight. Lactate was dissolved as stock solutions in PBS (10, 20, 50, 100, 200, and $500 \mu\text{M}$). Current-voltage characteristics of the devices were recorded using an Fs-Pro semiconductor parameter analyzer, PDA. The readout signal of the OECT at zero analyte concentration was the steady-state current obtained in PBS solution. After a steady baseline was obtained for the drain current, changes in response to subsequent additions of increasing concentrations of lactate solutions into the electrolyte were monitored as a function of time. For all the experiments, the volume of the solution was kept fixed at $10 \mu\text{l}$. The response of the device to lactate was normalized to allow for an accurate comparison between different devices. The normalized response (NR) was determined by the following equation, which considers the current output after it reaches a steady-state value

$$\text{NR} = \left| \frac{I_{\text{DS}} - I_{\text{DS},0}}{I_{\text{DS},0}} \right|$$

where $I_{DS,0}$ and I_{DS} are the current outputs in the absence of any analyte (baseline) and after the addition of a specific concentration of analyte, respectively.

The selectivity of the fiber sensor device is verified by adding non-relevant biomolecules (10 μ l), such as urea, glucose, and fructose (dissolved in 1 \times PBS solution with a concentration of 100 μ M). The accuracy of the fiber OEET was determined by the coefficient of variance (CV) of different devices and calibrated using the method reported in the literature (68), where CV is defined as

$$CV = \frac{\sigma}{\mu}$$

where σ is the SD and μ is the mean.

Wearable device integration

The fiber OEET and fiber OTE were sewn into the fabric for integration using a commercially available embroidery needle. The semi-conducting fiber was first sewn on a knitted fabric. Silver slurry (MCN-ED002) was used and cured at 100°C for 10 min as the electrode. The OEET and OTE measurements were the same as the above methods.

Supplementary Materials

This PDF file includes:

Figs S1 to S38

Tables S1 to S7

Appendix 1

Legends for movies S1 and S2

Other Supplementary Material for this manuscript includes the following:

Movies S1 and S2

REFERENCES AND NOTES

- J. Xiong, J. Chen, P. S. Lee, Functional fibers and fabrics for soft robotics, wearables, and human-robot interface. *Adv. Mater.* **33**, e2002640 (2020).
- A. R. Bunsell, J. W. S. Hearle, The fatigue of synthetic polymeric fibers. *J. Appl. Polym. Sci.* **18**, 267–291 (1974).
- T. D. Y. Kozai, N. B. Langhals, P. R. Patel, X. Deng, H. Zhang, K. L. Smith, J. Lahann, N. A. Kotov, D. R. Kipke, Ultrasmall implantable composite microelectrodes with bioactive surfaces for chronic neural interfaces. *Nat. Mater.* **11**, 1065–1073 (2012).
- H. Bai, S. Li, J. Barreiros, Y. Tu, C. R. Pollock, R. F. Shepherd, Stretchable distributed fiber-optic sensors. *Science* **370**, 848–852 (2020).
- J. Li, Y. Liu, L. Yuan, B. Zhang, E. S. Bishop, K. Wang, J. Tang, Y.-Q. Zheng, W. Xu, S. Niu, L. Beker, T. L. Li, G. Chen, M. Diyaolu, A.-L. Thomas, V. Mottini, J. B. H. Tok, J. C. Y. Dunn, B. Cui, S. P. Paçca, Y. Cui, A. Habtezion, X. Chen, Z. Bao, A tissue-like neurotransmitter sensor for the brain and gut. *Nature* **606**, 94–101 (2022).
- W. Margulis, Integration of optoelectronics into fibres enhances textiles. *Nature* **560**, 170–171 (2018).
- A. I. Boukai, Y. Bunimovich, J. Tahir-Kheli, J.-K. Yu, W. A. Goddard III, J. R. Heath, Silicon nanowires as efficient thermoelectric materials. *Nature* **451**, 168–171 (2008).
- A. J. Kulkarni, M. Zhou, F. J. Ke, Orientation and size dependence of the elastic properties of zinc oxide nanobelts. *Nanotechnology* **16**, 2749–2756 (2005).
- X. Zhao, X. Chen, H. Yuk, S. Lin, X. Liu, G. Parada, Soft materials by design: Unconventional polymer networks give extreme properties. *Chem. Rev.* **121**, 4309–4372 (2021).
- Z. Chen, T. Zhang, C.-T. Chen, S. Yang, Z. Lv, L. Cao, J. Ren, Z. Shao, L.-B. Jiang, S. Ling, Mechanically and electrically biocompatible hydrogel ionotronic fibers for fabricating structurally stable implants and enabling noncontact physioelectrical modulation. *Mater. Horiz.* **9**, 1735–1749 (2022).
- T. Matsuda, R. Kawakami, R. Namba, T. Nakajima, J. P. Gong, Mechanoresponsive self-growing hydrogels inspired by muscle training. *Science* **363**, 504–508 (2019).
- J.-Y. Sun, X. Zhao, W. R. K. Illeperuma, O. Chaudhuri, K. H. Oh, D. J. Mooney, J. J. Vlassak, Z. Suo, Highly stretchable and tough hydrogels. *Nature* **489**, 133–136 (2012).
- Y. Ye, Y. Zhang, Y. Chen, X. Han, F. Jiang, Cellulose nanofibrils enhanced, strong, stretchable, freezing-tolerant ionic conductive organohydrogel for multi-functional sensors. *Adv. Funct. Mater.* **30**, 2003430 (2020).
- Y. Shrike, A. Khademhosseini, Advances in engineering hydrogels. *Science* **356**, 497–499 (2017).
- Z. Songlin, Z. Yihao, L. Alberto, D. Yibing, L. Mingyang, Z. Mengjuan, Q. Hao, Z. Xun, Z. Peng, Z. You-Liang, C. Jun, T. Swee Ching, Biomimetic spinning of soft functional fibers via spontaneous phase separation. *Nat. Electron.* **6**, 338–348 (2023).
- J. Xue, R. Wang, X. Chen, C. Yao, X. Jin, K.-L. Wang, W. Huang, T. Huang, Y. Zhao, Y. Zhai, D. Meng, S. Tan, R. Liu, Z.-K. Wang, C. Zhu, K. Zhu, M. C. Beard, Y. Yan, Y. Yang, Reconfiguring the band-edge states of photovoltaic perovskites by conjugated organic cations. *Science* **371**, 636–640 (2021).
- Y.-Q. Zheng, Y. Liu, D. Zhong, S. Nikzad, S. Liu, Z. Yu, D. Liu, H.-C. Wu, C. Zhu, J. Li, H. Tran, J. B. H. Tok, Z. Bao, Monolithic optical microlithography of high-density elastic circuits. *Science* **373**, 88–94 (2021).
- O. Bubnova, Z. U. Khan, H. Wang, S. Braun, D. R. Evans, M. Faretto, P. Hojati-Talemi, D. Dagnelund, J.-B. Arlin, Y. H. Geerts, S. Desbief, D. W. Breiby, J. W. Andreasen, R. Lazzaroni, W. M. Chen, I. Zozoulenko, M. Fahlman, P. J. Murphy, M. Berggren, X. Crispin, Semi-metallic polymers. *Nat. Mater.* **13**, 190–194 (2014).
- Y. Jiang, Z. Zhang, Y.-X. Wang, D. Li, C.-T. Coen, E. Hwaun, G. Chen, H.-C. Wu, D. Zhong, S. Niu, W. Wang, A. Saberi, J.-C. Lai, Y. Wu, Y. Wang, A. A. Trotsyuk, K. Y. Loh, C.-C. Shih, W. Xu, K. Liang, K. Zhang, Y. Bai, G. Gurusankar, W. Hu, W. Jia, Z. Cheng, R. H. Dauskardt, G. C. Gurtner, J. B. H. Tok, K. Deisseroth, I. Soltesz, Z. Bao, Topological supramolecular network enabled high-conductivity, stretchable organic bioelectronics. *Science* **375**, 1411–1417 (2022).
- Y. Kim, H. Noh, B. D. Paulsen, J. Kim, I.-Y. Jo, H. Ahn, J. Rivnay, M.-H. Yoon, Strain-engineering induced anisotropic crystallite orientation and maximized carrier mobility for high-performance microfiber-based organic bioelectronic devices. *Adv. Mater.* **33**, e2007550 (2021).
- B. Fang, J. Yan, D. Chang, J. Piao, K. M. Ma, Q. Gu, P. Gao, Y. Chai, X. Tao, Scalable production of ultrafine polyaniline fibres for tactile organic electrochemical transistors. *Nat. Commun.* **13**, 2101 (2022).
- M. Li, J. Zheng, X. Wang, R. Yu, Y. Wang, Y. Qiu, X. Cheng, G. Wang, G. Chen, K. Xie, J. Tang, Light-responsive self-strained organic semiconductor for large flexible OFET sensing array. *Nat. Commun.* **13**, 4912 (2022).
- J. Xu, S. Wang, G.-J. N. Wang, C. Zhu, S. Luo, L. Jin, X. Gu, S. Chen, V. R. Feig, J. W. F. To, S. Rondeau-Gagné, J. Park, B. C. Schroeder, C. Lu, J. Y. Oh, Y. Wang, Y.-H. Kim, H. Yan, R. Sinclair, D. Zhou, G. Xue, B. Murmann, C. Linder, W. Cai, J. B. H. Tok, J. W. Chung, Z. Bao, Highly stretchable polymer semiconductor films through the nanoconfinement effect. *Science* **355**, 59–64 (2017).
- Y. Zhao, A. Gumyusenge, J. He, G. Qu, W. W. McNutt, Y. Long, H. Zhang, L. Huang, Y. Diao, J. Mei, Continuous melt-drawing of highly aligned flexible and stretchable semiconducting microfibers for organic electronics. *Adv. Funct. Mater.* **28**, 1705584 (2017).
- X. Yan, M. Xiong, X. Y. Deng, K. K. Liu, J. T. Li, X. Q. Wang, S. Zhang, N. Prine, Z. Zhang, W. Huang, Y. Wang, J. Y. Wang, X. Gu, S. K. So, J. Zhu, T. Lei, Approaching disorder-tolerant semiconducting polymers. *Nat. Commun.* **12**, 5723 (2021).
- P. Li, J. Shi, Y. Lei, Z. Huang, T. Lei, Switching p-type to high-performance n-type organic electrochemical transistors via doped state engineering. *Nat. Commun.* **13**, 5970 (2022).
- H. Jia, Z. Huang, P. Li, S. Zhang, Y. Wang, J.-Y. Wang, X. Gu, T. Lei, Engineering donor-acceptor conjugated polymers for high-performance and fast-response organic electrochemical transistors. *J. Mater. Chem. C* **9**, 4927–4934 (2021).
- R. Noriega, J. Rivnay, K. Vandewal, F. P. Koch, N. Stingelin, P. Smith, M. F. Toney, A. Salleo, A general relationship between disorder, aggregation and charge transport in conjugated polymers. *Nat. Mater.* **12**, 1038–1044 (2013).
- R. Venkatesh, Y. Zheng, C. Viersen, A. Liu, C. Silva, M. Grover, E. Reichmanis, Data science guided experiments identify conjugated polymer solution concentration as a key parameter in device performance. *ACS Mater. Lett.* **3**, 1321–1327 (2021).
- V. Rahul, Z. Yulong, L. L. Aaron, Z. Haoqun, S. Carlos, J. T. Christopher, A. G. Marthia, J. C. Meredith, R. Elsa, Overlap concentration generates optimum device performance for DPP-based conjugated polymers. *Org. Electron.* **117**, 106779 (2023).
- S. Bounoua, E. Lemaire, J. Férec, G. Ausias, P. Kuzhir, Shear-thinning in concentrated rigid fiber suspensions: Aggregation induced by adhesive interactions. *J. Rheol.* **60**, 1279–1300 (2016).
- G. W. S. Blair, J. C. Hening, A. Wagstaff, The flow of cream through narrow glass tubes. *J. Phys. Chem.* **43**, 853–864 (1939).
- J. J. Kwok, G. Vishwanathan, K. S. Park, B. B. Patel, D. Zhao, G. Juarez, Y. Diao, Understanding the aggregation and flow response of donor-acceptor conjugated polymers. *Macromolecules* **55**, 10153–10166 (2022).
- M. Ponçot, J. Martin, S. Chaudemanche, O. Ferry, T. Schenk, J. P. Tinnes, D. Chapron, I. Royaud, A. Dahoun, P. Bourson, Complementarities of high energy WAXS and Raman spectroscopy measurements to study the crystalline phase orientation in polypropylene blends during tensile test. *Polymer* **80**, 27–37 (2015).
- H.-C. W. Roland Boese, D. Bläser, The melting point alternation in the short-chain n-alkanes: Single-crystal X-ray analyses of propane at 30 K and of n-butane to n-nonane at 90 K. *Angew. Chem. Int. Ed. Engl.* **38**, 988–992 (1999).

36. T. F. Yohei Yamamoto, Y. Suna, N. Ishii, A. Saeki, S. Seki, S. Tagawa, M. Taniguchi, T. Kawai, T. Aida, Photoconductive coaxial nanotubes of molecularly connected electron donor and acceptor layers. *Science* **314**, 1761–1764 (2006).
37. K. A. O'Leary, D. R. Paul, Physical properties of poly(n-alkyl acrylate) copolymers. Part 1. Crystalline/crystalline combinations. *Polymer* **47**, 1226–1244 (2006).
38. J. Rivnay, S. C. Mannsfeld, C. E. Miller, A. Salleo, M. F. Toney, Quantitative determination of organic semiconductor microstructure from the molecular to device scale. *Chem. Rev.* **112**, 5488–5519 (2012).
39. A. M. Hindleleh, R. J. Hosemann, Paracrystals representing the physical state of matter. *J. Phys. C: Solid State Phys.* **21**, 4155 (1988).
40. M. Li, A. H. Balawi, P. J. Leenaers, L. Ning, G. H. L. Heintges, T. Marszalek, W. Pisula, M. M. Wienk, S. C. J. Meskers, Y. Yi, F. Laquai, R. A. J. Janssen, Impact of polymorphism on the optoelectronic properties of a low-bandgap semiconducting polymer. *Nat. Commun.* **10**, 2867 (2019).
41. Z. Wang, Z. Ma, L. Li, Flow-induced crystallization of polymers: Molecular and thermodynamic considerations. *Macromolecules* **49**, 1505–1517 (2016).
42. A. Abutaha, P. Kumar, E. Yildirim, W. Shi, S.-W. Yang, G. Wu, K. Hippalgaonkar, Correlating charge and thermoelectric transport to paracrystallinity in conducting polymers. *Nat. Commun.* **11**, 1737 (2020).
43. F. Guo, Y. Ren, J. Sha, Z. Cao, T. Ma, Y. Chong, H. Niu, Y. Li, T. Li, B. Ren, Solubility, molecular simulation, Hansen solubility parameter and thermodynamic properties of citiolone in thirteen organic pure solvents at different temperatures. *J. Chem. Thermodyn.* **164**, 106624 (2022).
44. E. F. Javier Jimenez, Mapping wet vs gel spinning in Hansen space. *Polymer* **230**, 124079 (2021).
45. J. Kim, G. Zhang, M. Shi, Z. Suo, Fracture, fatigue, and friction of polymers in which entanglements greatly outnumber cross-links. *Science* **374**, 212–216 (2021).
46. P. J. W. Somerville, A. H. Balzer, G. Lecroy, L. Guio, Y. Wang, J. W. Onorato, N. A. Kukhta, X. Gu, A. Salleo, N. Stingelin, C. K. Luscombe, Influence of side chain interdigitation on strain and charge mobility of planar indacenodithiophene copolymers. *ACS Polym. Au* **3**, 59–69 (2022).
47. D. M. DeLongchamp, R. J. Kline, E. K. Lin, D. A. Fischer, L. J. Richter, L. A. Lucas, M. Heeney, I. McCulloch, J. E. Northrup, High carrier mobility polythiophene thin films: Structure determination by experiment and theory. *Adv. Mater.* **19**, 833–837 (2007).
48. H. N. S. Yuan, L. Angela, T. Helen, Designing for softness in semiconducting conjugated polymers. *Acc. Mater. Res.* **4**, 205–208 (2023).
49. R. J. Kline, M. D. Dean, A. F. Daniel, K. L. Eric, J. R. Lee, L. C. Michael, F. T. Michael, H. Martin, M. Iain, Critical role of side-chain attachment density on the order and device performance of polythiophenes. *Macromolecules* **40**, 7960–7965 (2007).
50. Y. Liu, A. F. McGuire, H.-Y. Lou, T. L. Li, J. B. H. Tok, B. Cui, Z. Bao, Soft conductive micropillar electrode arrays for biologically relevant electrophysiological recording. *Proc. Natl. Acad. Sci. U.S.A.* **115**, 11718–11723 (2018).
51. Y. Zhao, S. S. You, A. Zhang, J.-H. Lee, J. Huang, C. M. Lieber, Scalable ultrasmall three-dimensional nanowire transistor probes for intracellular recording. *Nat. Nanotechnol.* **14**, 783–790 (2019).
52. C. Xie, J. Liu, T.-M. Fu, X. Dai, W. Zhou, C. M. Lieber, Three-dimensional macroporous nanoelectronic networks as minimally invasive brain probes. *Nat. Mater.* **14**, 1286–1292 (2015).
53. G. Hong, C. M. Lieber, Novel electrode technologies for neural recordings. *Nat. Rev. Neurosci.* **20**, 330–345 (2019).
54. S. Guan, J. Wang, X. Gu, Y. Zhao, R. Hou, H. Fan, L. Zou, L. Gao, M. Du, C. Li, Y. Fang, Elastocapillary self-assembled neurotassels for stable neural activity recordings. *Sci. Adv.* **5**, eaav2842 (2019).
55. M. Z. Lijing Zheng, W. Baohu, Z. Li, S. Sun, W. Peiyi, Conductance-stable liquid metal sheath-core microfibers for stretchy smart fabrics and self-powered sensing. *Sci. Adv.* **7**, eaabg4041 (2021).
56. Z. Chuang, W. Jiawei, Y. Jianhua, L. Xuqing, Advanced fiber materials for wearable electronics. *Adv. Fiber Mater.* **5**, 12–35 (2022).
57. J. Chen, W. Huang, D. Zheng, Z. Xie, X. Zhuang, D. Zhao, Y. Chen, N. Su, H. Chen, R. M. Pankow, Z. Gao, J. Yu, X. Guo, Y. Cheng, J. Strzalka, X. Yu, T. J. Marks, A. Facchetti, Highly stretchable organic electrochemical transistors with strain-resistant performance. *Nat. Mater.* **21**, 564–571 (2022).
58. H. Guo, C.-Y. Yang, X. Zhang, A. Motta, K. Feng, Y. Xia, Y. Shi, Z. Wu, K. Yang, J. Chen, Q. Liao, Y. Tang, H. Sun, H. Y. Woo, S. Fabiano, A. Facchetti, X. Guo, Transition metal-catalysed molecular n-doping of organic semiconductors. *Nature* **599**, 67–73 (2021).
59. J. Rivnay, S. Inal, A. Salleo, R. M. Owens, M. Berggren, G. G. Malliaras, Organic electrochemical transistors. *Nat. Rev. Mater.* **3**, 17086 (2018).
60. W. Huang, J. Chen, Y. Yao, D. Zheng, X. Ji, L.-W. Feng, D. Moore, N. R. Glavin, M. Xie, Y. Chen, R. M. Pankow, A. Surendran, Z. Wang, Y. Xia, L. Bai, J. Rivnay, J. Ping, X. Guo, Y. Cheng, T. J. Marks, A. Facchetti, Vertical organic electrochemical transistors for complementary circuits. *Nature* **613**, 496–502 (2023).
61. A.-M. Pappa, V. F. Curto, M. Braendlein, X. Strakoskas, M. J. Donahue, M. Focchi, G. G. Malliaras, R. M. Owens, Organic transistor arrays integrated with finger-powered microfluidics for multianalyte saliva testing. *Adv. Healthc. Mater.* **5**, 2295–2302 (2016).
62. D. Jiang, C. Xu, Q. Zhang, Y. Ye, Y. Cai, K. Li, Y. Li, X. Huang, Y. Wang, In-situ preparation of lactate-sensing membrane for the noninvasive and wearable analysis of sweat. *Biosens. Bioelectron.* **210**, 114303 (2022).
63. X. Yang, T. Fu, P. Kota, M. Tjia, C. Nguyen, J.-C. Chiao, Lactate sensors on flexible substrates. *Biosensors* **6**, 48 (2016).
64. S. Demuru, C.-H. Huang, K. Parvez, R. Worsley, G. Mattana, B. Piro, V. Noël, C. Casiraghi, D. Briand, All-inkjet-printed graphene-gated organic electrochemical transistors on polymeric foil as highly sensitive enzymatic biosensors. *ACS Appl. Nano Mater.* **5**, 1664–1673 (2022).
65. A. M. Pappa, D. Ohayon, A. Giovannitti, I. P. Maria, A. Savva, I. Uguz, J. Rivnay, I. McCulloch, R. M. Owens, S. Inal, Direct metabolite detection with an n-type accumulation mode organic electrochemical transistor. *Sci. Adv.* **4**, eaat0911 (2018).
66. M. M. Ito, A. H. Gibbons, D. Qin, D. Yamamoto, H. Jiang, D. Yamaguchi, K. Tanaka, E. Sivaniah, Structural colour using organized microfibrillation in glassy polymer films. *Nature* **570**, 363–367 (2019).
67. Materials Studio v6.0.0 Accelrys Software Inc, S. D., CA, 2011.
68. Gaussian 16, Revision A.03, M. J. Frisch, G. W. Trucks, H. B. Schlegel, G. E. Scuseria, M. A. Robb, J. R. Cheeseman, G. Scalmani, V. Barone, B. Mennucci, G. A. Petersson, H. Nakatsuji, M. Caricato, X. Li, H. P. Hratchian, A. F. Izmaylov, J. Bloino, G. Zheng, J. L. Sonnenberg, M. Hada, M. Ehara, K. Toyota, R. Fukuda, J. Hasegawa, M. Ishida, T. Nakajima, Y. Honda, O. Kitao, H. Nakai, T. Vreven, J. A. Montgomery, Jr., J. E. Peralta, F. Ogliaro, M. Bearpark, J. J. Heyd, E. Brothers, K. N. Kudin, V. N. Staroverov, R. Kobayashi, J. Normand, K. Raghavachari, A. Rendell, J. C. Burant, S. S. Iyengar, J. Tomasi, M. Cossi, N. Rega, J. M. Millam, M. Klene, J. E. Knox, J. B. Cross, V. Bakken, C. Adamo, J. Jaramillo, R. Gomperts, R. E. Stratmann, O. Yazyev, A. J. Austin, R. Cammi, C. Pomelli, J. W. Ochterski, R. L. Martin, K. Morokuma, V. G. Zakrzewski, G. A. Voth, P. Salvador, J. J. Dannenberg, S. Dapprich, A. D. Daniels, O. Farkas, J. B. Foresman, J. V. Ortiz, J. Cioslowski, and D. J. Fox, Gaussian Inc., Wallingford CT, 2016.
69. S. Zhang, M. U. Ocheje, L. Huang, L. Galuska, Z. Cao, S. Luo, Y. H. Cheng, D. Ehlenberg, R. B. Goodman, D. Zhou, Y. Liu, Y. C. Chiu, J. D. Azoulay, S. Rondeau-Gagné, X. Gu, The critical role of electron-donating thiophene groups on the mechanical and thermal properties of donor-acceptor semiconducting polymers. *Adv. Electron. Mater.* **5**, 1800899 (2019).
70. A. X. Chen, A. T. Kleinschmidt, K. Choudhary, D. J. Lipomi, Beyond stretchability: Strength, toughness, and elastic range in semiconducting polymers. *Chem. Mater.* **32**, 7582–7601 (2020).
71. Z. Wei, X. Wang, B. Seo, X. Luo, Q. Hu, J. Jones, M. Zeller, K. Wang, B. M. Savoie, K. Zhao, L. Dou, Side-chain control of topochemical polymer single crystals with tunable elastic modulus. *Angew. Chem. Int. Ed. Engl.* **61**, e202213840 (2022).
72. S. E. Root, S. Savagatrup, A. D. Printz, D. Rodriguez, D. J. Lipomi, Mechanical properties of organic semiconductors for stretchable, highly flexible, and mechanically robust electronics. *Chem. Rev.* **117**, 6467–6499 (2017).

Acknowledgments

Funding: This work is supported by the National Key R&D Program of China (2022YFE0130600), Beijing Natural Science Foundation (JQ22006), and National Natural Science Foundation of China (22075001 and 92156019). Z.Z. thanks the China Postdoctoral Science Foundation (2021 M700190 and 2021TQ0001) and the Boya Postdoctoral Fellowship of Peking University. We acknowledge the Molecular Materials and Nanofabrication Laboratory (MMNL) in the College of Chemistry and Electron Microscopy Laboratory of Peking University for the use of instruments. The computational part is supported by High-performance Computing Platform of Peking University. **Author contributions:** T.L. and Z.Z. conceived the project. Z.Z. performed fiber and device fabrication and characterization. J.C., X.L., X.P., K.-K.L., and G.L. synthesized the polymers. P.L. and M.X. performed some characterization. X.W. performed the SEM measurements. X.P. and X.-Y.D. performed DFT calculations. L.Z. and Y.S. performed some mechanical tests of the fibers. W.S. performed the calculation of fluid mechanics inside the needle. Z.M. and S.L. performed the cell culture experiments. Z.Z. and T.L. wrote the manuscript. All the authors revised and approved the manuscript. **Competing interests:** The authors declare that they have no competing interests. **Data and materials availability:** All data needed to evaluate the conclusions in the paper are present in the paper and/or the Supplementary Materials.

Submitted 31 July 2023
Accepted 26 February 2024
Published 3 April 2024
10.1126/sciadv.adk0647